# *In Situ* Characterization of a Graphite Electrode in a Secondary Lithium-Ion Battery Using Raman Microscopy

J.-C. PANITZ,* F. JOHO, and P. NOVÁK

*General Energy Research Department, Paul Scherrer Institute, CH-5232 Villigen PSI, Switzerland*

**A Raman microscopy study of lithium intercalation into the graphite electrode of a lithium-ion battery is presented. An *in situ* spectroelectrochemical cell was designed for direct observation of the electrode/electrolyte interface. The performance of this cell is discussed in terms of the results of a calibration experiment performed at a single defined point on the electrode surface. The electrode was made of TIMREX SFG 44 synthetic graphite with polyvinylidene fluoride binder. The electrolyte was lithium perchlorate, $LiClO_4$, dissolved in a mixture of ethylene carbonate and dimethyl carbonate. In the region of the carbonyl stretching vibrational modes of the electrolyte components, changes in the band profile have been observed. At electrode potentials negative to 180 mV vs. $Li/Li^+$, a new band evolved at about 1850 $cm^{-1}$. This band has tentatively been assigned to a complex between lithium ions and decomposition products of the ethylene carbonate electrolyte component. The maximum intensity of this new band is observed at 5 mV vs. $Li/Li^+$; its intensity decreases with increasing potential upon lithium de-intercalation. Raman mapping of the graphite electrode under potentiostatic conditions indicates that lithium intercalation does not proceed homogeneously over the graphite electrode surface at a potential of 200 mV vs. $Li/Li^+$. An additional Raman mapping study was performed under galvanostatic conditions. With this method, the presence of "blind spots" on the electrode surface can be detected. These points lag behind in the process of lithium intercalation. Furthermore, information on changes in the carbon component of the electrode can be inferred from these measurements.**

Index Headings: **Raman microscopy; Lithium-ion battery; Lithium intercalation; Carbon; Graphite.**

## INTRODUCTION

Secondary lithium-ion batteries have been successfully introduced into the market in recent years. In these batteries, lithiated metal oxides such as $Li_xCoO_2$, $Li_xNiO_2$, or $Li_xMn_2O_4$ are used as the positive electrode material, while carbon serves as the negative electrode material. For the electrolyte, lithium salts dissolved in nonaqueous solvents are employed. Recent reviews of developments in this field are available from Dahn et al.[1] and Winter et al.[2] Today the energy density of lithium-ion batteries is considerably higher than that of the nickel-metal hydride (NiMH) or NiCd system, yet a potential for further improvements exists. One open challenge is the rather large irreversible charge (in the technical literature called "charge loss") encountered during the first charge/discharge cycle of the carbon electrode. It is assumed that this charge loss is mainly due to decomposition of the electrolyte on the negative carbon electrode.[2] A protective film called solid electrolyte interphase (SEI) is formed that allows $Li^+$-ion transfer but prevents electron transfer. This film has been observed *ex situ*, e.g., with the use of transmission electron microscopy and small-angle electron diffraction.[3] In order to understand the processes taking place during the first cycle, several studies have been performed *in situ*. For example, atomic force microscopy (AFM) has been applied to study SEI formation on HOPG (highly ordered pyrolytic graphite),[4,5] but experimental difficulties were reported when attempts were made to apply this technique to synthetic graphite powder.[4] Methods such as X-ray diffraction,[6–8] Fourier transform infrared (FT-IR) spectroscopy,[9] Raman spectroscopy,[10–12] electron spin resonance,[13] and differential electrochemical mass spectrometry (DEMS)[14,15] have been employed so far to study lithium intercalation into carbon electrodes *in situ*, in addition to electrochemical techniques.[16,17]

Raman spectroscopy is especially well suited for the characterization of carbon materials. The Raman spectrum of graphite has been discussed by several authors, and the spectral features observed have been related to the structure of the materials investigated.[18–22] The prominent feature in the Raman spectra of graphitic carbons is the $E_{2g}{}^2$ mode at 1580 $cm^{-1}$. Upon lithium intercalation, this band shifts to higher wavenumbers. The $E_{2g}{}^2$ mode broadens with increasing lithium intercalation and finally splits into two components. This behavior mirrors the formation of a layered intercalation compound consisting of alternating graphene sheets and lithium layers. In lithium-intercalated graphite compounds, we distinguish between two types of graphene layers: those adjacent only to other graphene layers are called interior graphene layers, and those adjacent to a lithium layer are called boundary layers. The high-wavenumber component of the split $E_{2g}$ mode is assigned to the $E_{2g}{}^{2(i)}$ mode originating from the interior graphene layers of the lithium-intercalated graphite. The corresponding low-wavenumber component is assigned to the same vibrational mode in the boundary layers of the lithium-intercalated graphite, and designated as $E_{2g}{}^{2(b)}$. According to Solin,[23] the intensity ratio of these bands may be used to deduce the staging index of the lithium intercalation compound under investigation. A more detailed description of these observations can be found in the work of Inaba et al.[10] *In situ* studies of carbon electrodes using Raman spectroscopy have shown that with this method one can indeed monitor the different stages of lithium intercalation.[10,12] The reverse process of lithium de-intercalation can be monitored in the same way.

Here, we present results from an *in situ* Raman microscopy study of a graphite electrode. Several cells were examined, revealing good reproducibility of the measurements. In the following, one representative set of results is discussed in detail. Our aim was to perform a direct

Received 21 January 1999; accepted 10 May 1999.
* Author to whom correspondence should be sent.


0003-7028/99/5310-1188$2.00/0

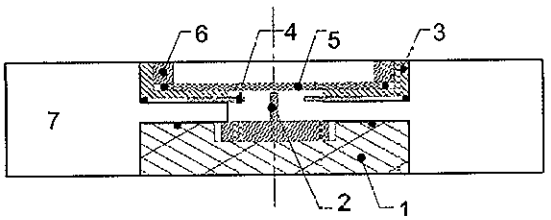


FIG. 1. Scheme of the *in situ* cell. (1) Stainless steel body contacting the working electrode; (2) holder for the graphite working electrode (the graphite is deposited on top of the holder); (3) current collector for the lithium counter electrode; (4) counter-electrode (lithium foil); (5) sapphire window; (6) retainer ring; (7) cell body made of (poly)-propylene.

investigation of the interface between electrolyte and electrode in order to gain a better understanding of the electrochemical processes involved. In this way valuable information on the SEI film should be made available, depending on its thickness. By using a confocal microscope, we have improved the spatial resolution over that reported in published work.[10-12] Thus, the lithium intercalation process has been monitored at a selected area of the graphite electrode. In contrast to previous investigators,[10,12] we do not restrict our discussion to the bands attributed to carbon and lithium-intercalated carbon compounds. The vibrational bands of the electrolyte solvent in the vicinity of the electrode surface were taken into account as well. Since the electrode surface is wetted by the electrolyte, an interpretation of the results obtained should rely on information obtained for all components of the system investigated. The experiment performed also served to validate the new design of our *in situ* electrochemical cell. Further, it was our intention to extend existing methods towards a spatially resolved spectroscopy of the lithium intercalation process in carbon electrodes composed of the materials used in real world batteries. Up to the present, Raman imaging has been applied only to glassy carbon covered with water[24] and to a lithium cell composed of lithium, a polymer electrolyte, and vanadium oxide.[25] We have performed Raman mapping experiments on graphite electrodes, under both galvanostatic and potentiostatic conditions. In this article, we report first results and compare the data obtained under these two conditions.

## EXPERIMENTAL

**Electrochemistry.** The *in situ* cell employed is shown schematically in Fig. 1. The composite working electrode was a thin film of graphite [TIMREX SFG 44, TIMCAL AG, mixed with 5 wt % polyvinylidene fluoride (PVDF), obtained from Aldrich], which was deposited on the end-face of a stainless steel rod (2) and typically had a mass of about 0.1 mg. The counter-electrode (4), was a lithium foil (Aldrich) pressed by a retainer ring (6) against the current collector (3). The electrolyte was 1 M $LiClO_4$ (Merck) in a 1:1 w/w mixture of ethylene carbonate (EC, Selectipur grade from Merck) and dimethyl carbonate (DMC, Selectipur grade from Merck). The electrolyte contained <10 ppm water as determined by Karl–Fischer titration. The cell components were assembled and hermetically sealed in a glove box under argon atmosphere.

The cell was placed under the microscope of the Raman system and connected to a standard potentiostat/galvanostat (AMEL, Milano, Model 2049) driven by QuickLog PC software (Strawberry Tree Inc.). The experiments were performed at room temperature. Typically, the cell was cycled with a current of 10 μA (~100 μA/mg of graphite) between the potential limits of the carbon electrode of 1500 and 5 mV vs. $Li/Li^+$. Throughout this paper, the potentials given are potentials measured vs. the $Li/Li^+$ couple.

**Raman Measurements.** Raman spectroscopy was performed with a confocal Raman microscope (LabRam, DILOR/Instruments S.A.), with the use of the 530.901 nm line of an external $Kr^+$ ion laser (Innova 302, Coherent Inc.). The components of the composite electrode were first examined *ex situ*. Measurements under *in situ* conditions were performed in the cell shown in Fig. 1. With a microscope objective providing 50× magnification [Olympus ULWD, 8 mm working distance, numerical aperture (NA) = 0.55], it is possible to obtain Raman spectra from layers located up to 4 mm below the sapphire window. With the pinhole diameter of the confocal microscope adjusted to 200 μm, the lateral resolution is 4 μm, according to the specifications of the manufacturer. However, it should be pointed out that some optical throughput and spatial resolution are lost due to the fact that the laser beam focused on the electrode passes three media of different indices of refraction.[26] Laser power was limited to 3 mW at the sample in order to avoid local heating of the graphite particles. With higher power levels, disruption of the electrode surface was observed in preliminary experiments. Also, bubbles may then form during the charging and discharging cycles and cause problems in mapping experiments. The spacing between the sapphire window and the electrode surface is critical for a successful experiment; it was found that a distance of a few hundred micrometers is most appropriate. Data were recorded with a spectral resolution of 3 $cm^{-1}$. The band positions were calibrated by recording the spectrum of a neon lamp.

## RESULTS AND DISCUSSION

**Electrochemical Performance of the *in Situ* Cell.** A typical galvanostatic curve recorded during the first cycle with a current of 10 μA is shown in Fig. 2A. The different stages of lithium intercalation are clearly distinguishable by this method, with different plateaus corresponding to defined stages of lithium intercalation.[1,2] The Roman numbers in Fig. 2A indicate the different phases of our experiment. Starting from the open circuit potential, the electrode was charged to 120 mV vs. $Li/Li^+$ (region I). Then, the cell was left at open circuit for a period of 12 h; during that time the potential relaxed to 220 mV. After that, the charging was resumed (region II) and continued until the potential reached 5 mV. Then, the cell was again left for 120 min at open circuit, then discharged at 10 μA (region III).

The long-term performance of the cell is shown in Fig. 2B, where the charge accumulated in each cycle under continuous cycling at 10 μA is given for a period of 8 days. Due to the large ratio of electrolyte volume over electrode surface area in comparison to real batteries, the "charge loss" per cycle is relatively high. Nevertheless,

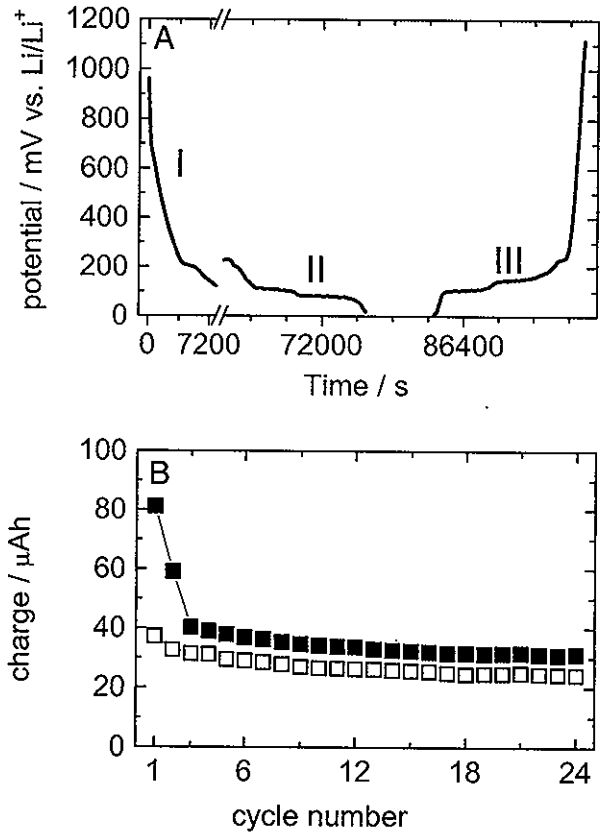


FIG. 2. (A) Galvanostatic charge/discharge curve of a SFG 44 graphite electrode recorded with a current of 10 μA (~100 μA/mg graphite) in the *in situ* cell (first cycle). After about 2 h, a potential of 120 mV was attained (region I). After an open circuit period of 12 h, the charging of the electrode was resumed (region II). In region III, the discharge of the graphite electrode is shown. (B) Electrochemical performance of the *in situ* cell at ~100 μA/mg graphite in a potential window from 1500 mV to 5 mV vs. Li/Li+ during 24 cycles (filled squares: charge; open squares: discharge).

the electrochemical performance of the *in situ* cell is quite satisfactory.

**Spectroscopic Performance of the *in Situ* Cell.** The effect of magnification of the microscope on the outcome of the Raman experiment is shown in Fig. 3. The upper trace shows the Raman spectrum recorded when the laser beam was focused on the graphite electrode at a potential of 800 mV with the use of an objective with 50× magnification. The confocal aperture was adjusted to a diameter of 200 μm. The lower spectrum was recorded under the same conditions, except for the use of an objective with 10× magnification. Both spectra have been normalized to the height of the strongest band at 900 $cm^{-1}$. The signal-to-noise (S/N) ratio is better for the spectrum recorded with 10× magnification, but the $E_{2g}^2$ mode of graphite is more readily distinguished from the signals due to electrolyte components when 50× magnification is used. Since the laser beam penetrates into the graphite material only to a very small depth, the better discrimination of the graphite band obtained when working with the 50× objective is simply due to the smaller volume of the focal cone sampled for the spectrum shown in the upper trace of Fig. 3. This observation also explains the difference in S/N ratio between the two spectra. Working with the 10× objective we sample a larger volume of a transparent liquid, resulting in a better S/N per unit measurement time, but less information from the interface between the electrolyte and the graphite electrode is obtained. All subsequent experiments were therefore performed with the use of the objective with 50× magnification.

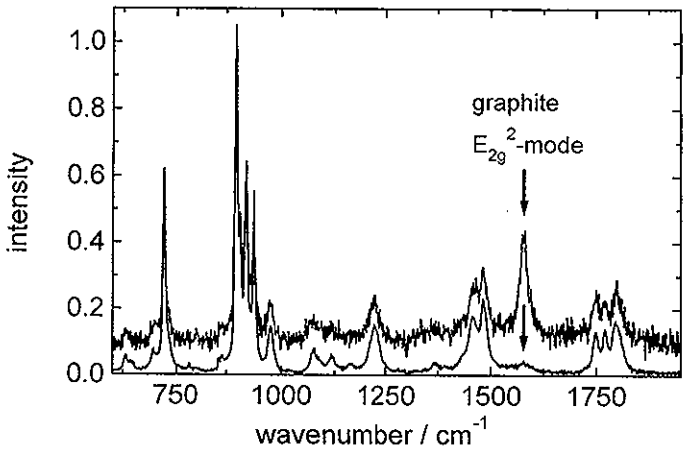


FIG. 3. Intensities of the graphite $E_{2g}^2$ band and signals of the electrolyte components. The S/N is better in the lower trace recorded with a microscope objective with 10× magnification, but the upper trace recorded with a 50× objective shows a better discrimination of the graphite signal from the electrolyte signals. Potential: 800 mV vs. Li/Li+.

***Ex Situ* Characterization of the Electrode Components.** Raman mapping was employed to characterize both the SFG 44 graphite and the PVDF binder used for electrode preparation. Trace A in Fig. 4 shows the Raman

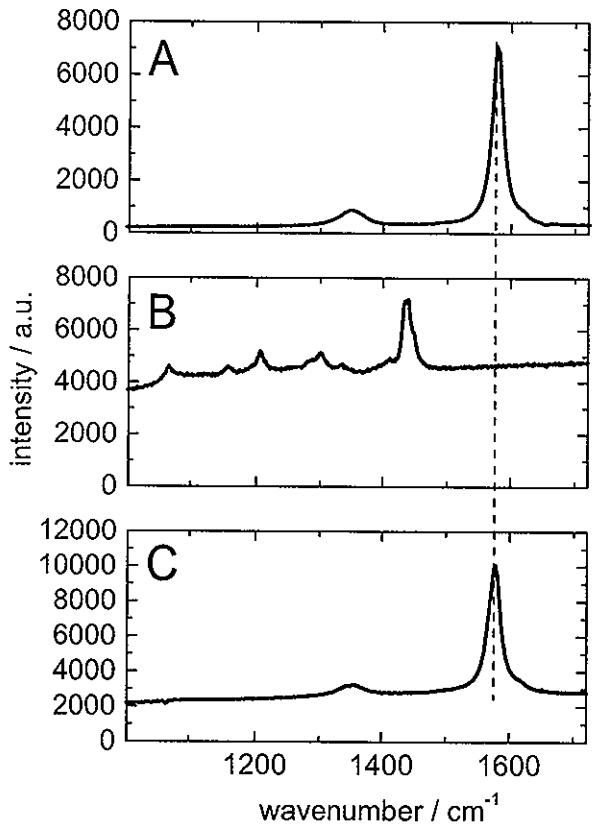


FIG. 4. Raman spectra of graphite SFG 44 (A), polyvinylidene fluoride (B), and the film electrode on top of the electrode support (C).

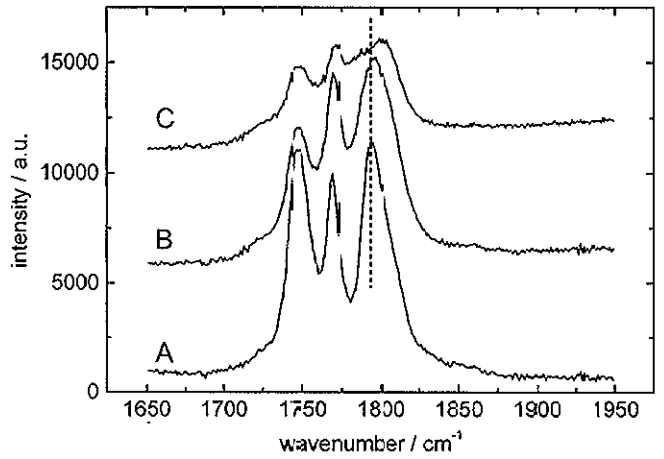


FIG. 5. Raman spectra of electrolyte solutions prepared from 50/50 v/v mixtures of ethylene carbonate and dimethyl carbonate. (*A*) Without $LiClO_4$; (*B*) 1 M $LiClO_4$; (*C*) 2 M $LiClO_4$. The dashed line indicates the shift in band position with increasing lithium concentration. Note also the changes in the band profiles.

spectrum of SFG 44, averaged over 144 points. The Raman spectrum of PVDF is shown in trace B, while the averaged Raman spectrum of the composite graphite electrode is given in trace C. The Raman bands of PVDF are superimposed on a strong background (trace B). The authors of a recent investigation[27] concluded that this background is due to interaction between low-wavenumber phonons and the high-wavenumber vibrations of the CH groups in PVDF. From an inspection of the Raman spectrum of the composite graphite electrode (Fig. 4C), we found that the position of the $E_{2g}^2$ mode of the graphite used did not change under the process conditions employed in electrode preparation. No bands assignable to PVDF appear in spectrum C, but the background emission has increased considerably over that in the Raman spectrum of neat SFG 44.

The electrolyte/solvent system used in the cell was investigated as well. The interaction of EC with $LiClO_4$, was investigated by Hyodo and Okabayashi[28] with the use of quantitative analysis of the Raman spectra. To our knowledge, similar investigations were not published for the solvent system used here. In Fig. 5, the Raman spectra of the EC/DMC mixture are shown. Only the region of the carbonyl stretching vibrations is displayed here. Spectrum A was recorded for the mixture of the solvents without the electrolyte salt, $LiClO_4$. Traces B and C show spectra of the solvents obtained after adding $LiClO_4$ in concentrations of 1 M and 2 M, respectively. In order to improve the readability of the figure, consecutive spectra were shifted vertically by constant amounts. Therefore, Fig. 5 does not reveal the evolution of the background level, which increases with increasing concentration of lithium salt. The shape change of the band profile is clearly visible. The intensity ratios of the bands constituting the profile change, as well as a shift in band position to higher wavenumbers, occur with increasing lithium perchlorate concentration. The band positions were calculated by using nonlinear least-squares (NLLSQ) fitting procedures implemented in the Origin 5.0 software package (Microcal Inc.). For spectrum A, the following values were found [full width at half maximum (FWHM) linewidths are given in brackets]: 1751 [15.3] $cm^{-1}$, 1772 [9.3] $cm^{-1}$, 1796 [12.3] $cm^{-1}$, and 1807 [21.6] $cm^{-1}$. The relative intensity ratios obtained from this calculations are 35.8:15.1:22.2:26.5. The band lowest in wavenumber is assigned to DMC; the other three bands are assigned to the EC component of the solvent mixture.[29] It is known that the C=O stretching vibration of EC is coupled by Fermi resonance to the overtone of the ring breathing vibration;[29–31] this factor accounts for the bands at 1772 and 1796 $cm^{-1}$. The third band at 1807 $cm^{-1}$ is assigned to a combination band.[31] The addition of $LiClO_4$, trace B, leads to the following new set of values for the band positions: 1751 [17.1] $cm^{-1}$, 1773 [11.5] $cm^{-1}$, 1797 [23.9] $cm^{-1}$, and 1810 [18.9] $cm^{-1}$. The relative intensity ratios are 22.6:17.3:45.1:14.6. Like the data shown in trace A, band profile B is best described by using four Voigt profiles. This approach no longer holds true for spectrum C, recorded with 2 M $LiClO_4$ dissolved in the EC/DMC mixture. Here, six bands were used instead in order to describe the experimental results. The band positions and corresponding linewidths (FWHM) are 1727 [11.1] $cm^{-1}$, 1751 [19.0] $cm^{-1}$, 1774 [14.1] $cm^{-1}$, 1789 [19.2] $cm^{-1}$, 1802 [17.9] $cm^{-1}$, and 1811 [16.7] $cm^{-1}$. The relative intensity ratios obtained are 1.9:26.2:18.5:18.9:20.5:14.0. We are well aware that the number of bands used in the last calculation (trace C) is an arbitrary choice. Detailed studies on the electrolyte used are under way and will be presented elsewhere. Here, we are interested only in obtaining reference data for comparison with data obtained in the model battery electrochemical cell under investigation.

The results presented in Fig. 5 can be summarized as follows: The band assigned to DMC changes in linewidth, but not in position. Upon addition of the lithium salt, the intensity of this band decreases relative to that of the bands of EC, which show significant shifts in wavenumber. We conclude, therefore, that the interaction of $Li^+$ is weaker with DMC than with EC. In the context of the present work, the observation that the EC band profile shifts to higher wavenumber with increasing $LiClO_4$ concentration is the most important one.

**Single-Point Raman Spectra Recorded During the First Cycle.** A selection of Raman spectra recorded during the first charge-discharge cycle is shown in Figs. 6 and 7. Data were recorded from the same spot throughout the experiment. The spectra recorded while charging the cell are given in Fig. 6. The diagram to the left corresponds to phase I of the experiment (cf. Fig. 2A); the spectra shown in the figure to the right were recorded in phase II of the first half-cycle. Band positions and linewidths calculated for the spectra shown in Figs. 6 and 7 are listed in Tables I and II, respectively. Traces A–D in Fig. 6 show that the intensity of the $E_{2g}^2$ mode decreases with decreasing electrode potential. In addition, a shift in band position from 1581 to 1592 $cm^{-1}$ is noted (see Table I). Trace E, recorded while the potential was in the range from 203 to 202 mV, shows a split of this band into two components, in agreement with results previously reported.[10] Within this subset of spectra, the bands assigned to the C=O stretching vibration of the EC and DMC solvent components undergo little change. It is known from DEMS experiments that ethylene is evolved in the potential window between 800 and 300 mV vs. $Li/Li^+$. This

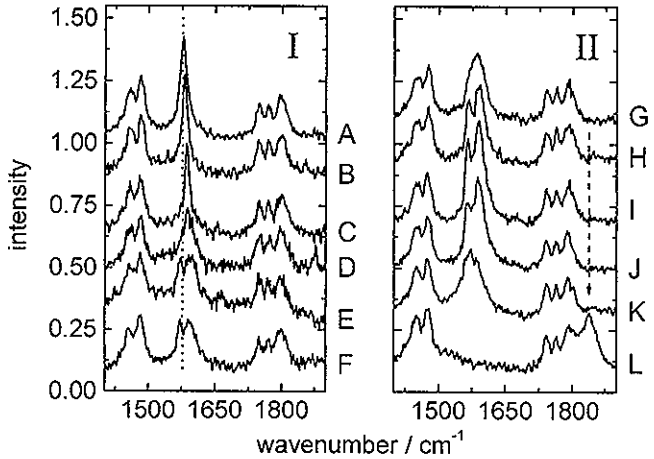


FIG. 6. (**I**) Raman spectra obtained at one specific point on the graphite electrode surface during the first charging half cycle. Spectra ***A–F*** were selected from the set of spectra recorded during charging from 702 mV (***A***) to 122 mV (***F***), corresponding to region I in the galvanostatic curve displayed in Fig. 2A. The dotted line is placed at the initial band position of the graphite signal. (**II**) Raman spectra recorded after the cell was left at open circuit for equilibration. Charging was resumed at a potential of 199 mV (spectrum ***G***) and ended during the measurement of spectrum ***L*** (region II of the galvanostatic curve, Fig. 2A). The dashed arrow indicates the position of the new feature observed. The potentials at which the spectra were recorded are listed in Table I.

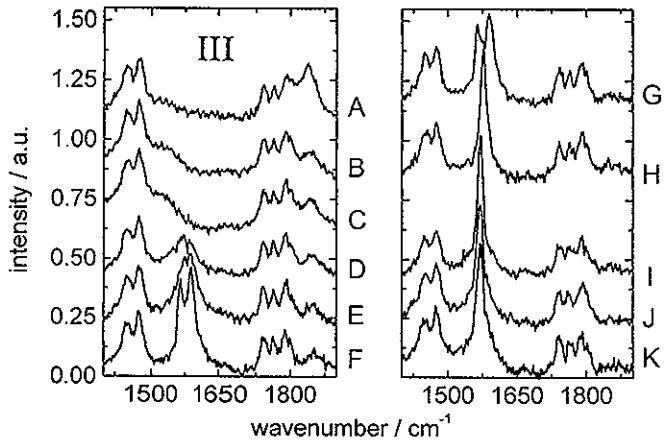


FIG. 7. Raman spectra obtained at one specific point on the graphite electrode surface during the first discharge half-cycle (lithium de-intercalation, region III in Fig. 2A). Spectra ***A–K*** were selected from the set of spectra recorded during discharge in the range from 5 mV (***A***) to 1210 mV (***K***). The potentials at which the spectra were recorded are listed in Table II.

result has been attributed to the formation of the SEI.[14] With the Raman technique, no spectral features of the SEI can be detected within this same potential window.

Spectrum G, recorded just before the charging was resumed (Fig. 2A, region II), shows one broad band in the range of 1550–1630 $cm^{-1}$. However, the band profile is best described by two Voigt profiles. The NLLSQ anal-

**TABLE I. Band positions and linewidths [full width at half-maximum, (FWHM)], both in $cm^{-1}$ for spectra recorded during lithium intercalation, as calculated by using curve fitting procedures. The linewidth is shown in square brackets. The intensity ratio is defined as $I(E_{2g}^{2(i)})/I(E_{2g}^{2(b)})$. This table refers to data shown in Fig. 6.**

| Spectrum[a] | Bands assigned to graphite and $Li_xC_y$ | | | | Int. ratio | Carbonyl stretching vibrations of DMC and EC | | | Observed in this work | |
|---|---|---|---|---|---|---|---|---|---|---|
| | | $(E_{2g}^{2(i)})$ | $(E_{2g}^{2(b)})$ | $(E_{2g}^{2})$ | | DMC | EC | EC | | |
| Region I | | | | | | | | | | |
| A (703–688) | | | | 1581 | | 1751 | 1773 | 1801 | | |
| | | | | [22.4] | | [16.2] | [12.1] | [26.2] | | |
| B (503–484) | | | | 1584 | | 1751 | 1773 | 1801 | | |
| | | | | [15.2] | | [15.6] | [10.1] | [28.2] | | |
| C (307–295) | | | | 1589 | | 1751 | 1772 | 1802 | | |
| | | | | [16.5] | | [14.5] | [9.5] | [31.7] | | |
| D (231–222) | 1541 | | | 1592 | | 1752 | 1775 | 1802 | | |
| | [42.6] | | | [30.7] | | [16.8] | [13.0] | [27.2] | | |
| E (203–202) | | 1574 | 1599 | | 8.5:25.7 | 1752 | 1772 | 1800 | | |
| | | [13.2] | [26.8] | | | [13.3] | [10.9] | [25.0] | | |
| F (162–154) | | 1573 | 1597 | | 7.2:27.1 | 1752 | 1772 | 1801 | | |
| | | [13.3] | [33.4] | | | [11.7] | [12.4] | [28.3] | | |
| Region II | | | | | | | | | | |
| G (199–188) | | 1582 | 1601 | | 16.3:24.2 | 1752 | 1774 | 1802 | | |
| | | [25.6] | [28.4] | | | [14.6] | [11.3] | [27.3] | | |
| H (167–152) | | 1576 | 1601 | | 8.8:31.1 | 1751 | 1773 | 1801 | | |
| | | [13.0] | [28.1] | | | [15.7] | [8.0] | [34.8] | | |
| I (145–138) | | 1574 | 1600 | | 7.7:43.1 | 1751 | 1773 | 1802 | | |
| | | [10.5] | [33.8] | | | [18.8] | [10.8] | [34.4] | | |
| J (135–125) | | 1574 | 1600 | | 6.8:37.6 | 1751 | 1773 | 1800 | | |
| | | [12.4] | [34.2] | | | [14.1] | [12.6] | [21.3] | | |
| K[b] (102–101) | | 1578 | 1602 | | 31.1:11.9 | 1752 | 1773 | 1799 | 1813 | 1858 |
| | | [44.5] | [37.8] | | | [14.4] | [11.5] | [19.5] | [11.3] | [17.5] |
| L (10–5) | 1536 | | | | | 1751 | 1773 | 1800 | 1816 | 1850 |
| | [97.7] | | | | | [15.4] | [12.0] | [22.7] | [32.0] | [38.3] |

[a] Spectra were recorded under galvanostatic conditions. Therefore, the potential range (in mV vs. $Li/Li^+$) covered during acquisition of each spectrum is listed after the identifying letter.

[b] Alternatively, the band assigned to lithium-intercalated graphite may be described (using a single Voigt profile, centered at 1583 $cm^{-1}$, and having a linewidth (FWHM) of 56.2 $cm^{-1}$. The correlation coefficient is only slightly lower in this calculation.

TABLE II. Band positions and linewidths for spectra recorded during lithium de-intercalation. The intensity ratio is defined as $I(E_{2g}^{2(i)})/I(E_{2g}^{2(b)})$. These spectra are shown in Fig. 7.

| Spectrum[a] | Bands assigned to graphite and $Li_xC_y$ | | | | Int. ratio | Carbonyl stretching vibration | | | Observed in this work | |
|---|---|---|---|---|---|---|---|---|---|---|
| | | $(E_{2g}^{2(i)})$ | $(E_{2g}^{2(b)})$ | $(E_{2g}^{2})$ | | | | | | |
| Region III | | | | | | | | | | |
| A (5–10) | 1536 | | | | | 1751 | 1773 | 1800 | 1815 | 1850 |
| | [97.7] | | | | | [15.4] | [12.0] | [22.7] | [32.0] | [38.3] |
| B (56–89) | 1537 | | | | | 1751 | 1773 | 1798 | 1812 | 1854 |
| | [63.2] | | | | | [21.0] | [13.2] | [23.2] | 20.6 | [47.5] |
| C (92–99) | 1534 | | | | | 1751 | 1774 | 1799 | 1813 | 1853 |
| | [62.7] | | | | | [24.7] | [15.3] | [19.3] | [18.6] | [59.6] |
| D (146–148) | 1555 | 1578 | 1602 | | 6.3:10.5 | 1751 | 1773 | 1799 | 1815 | 1858 |
| | [60.8] | [21.4] | [32.9] | | | [15.3] | [12.5] | [19.1] | [18.2] | [33.1] |
| E (159–159) | | 1578 | 1601 | | 21.4:25.2 | 1751 | 1774 | 1800 | 1815 | 1860 |
| | | [45.3] | [43.4] | | | [13.5] | [12.8] | [17.7] | [15.3] | [28.0] |
| F (183–191) | | 1573 | 1599 | | 9.6:35.3 | 1752 | 1773 | 1799 | 1812 | 1861 |
| | | [12.8] | [32.4] | | | [14.9] | [12.9] | [17.2] | [9.7] | [30.9] |
| G (206–219) | | 1574 | 1600 | | 12.5:29.7 | 1752 | 1774 | 1799 | 1812 | 1864 |
| | | [15.2] | [27.7] | | | [18.9] | [10.0] | [19.6] | [8.1] | [n.a.] |
| H (233–239) | | 1573 | 1599 | | 12.4:27.4 | 1752 | 1772 | 1800 | — | 1861 |
| | | [17.7] | [24.3] | | | [14.4] | [12.1] | [26.1] | — | 16.7 |
| I (446–572) | | | | 1581 | | 1752 | 1777 | 1799 | | |
| | | | | [12.5] | | [15.6] | [25.4] | [13.0] | | |
| J (741–924) | | | | 1580 | | 1750 | 1771 | 1802 | | |
| | | | | [26.4] | | [15.6] | [14.3] | [30.0] | | |
| K (1209–1305) | | | | 1581 | | 1751 | 1775 | 1799 | 1814 | |
| | | | | [25.0] | | [15.2] | [14.8] | [17.8] | [10.4] | |

[a] Spectra were recorded under galvanostatic conditions. Therefore, the potential range (in mV vs. $Li/Li^+$) covered during acquisition of each spectrum is listed after the identifying letter.

ysis revealed that the intensity ratio of these two components changed during the period at open circuit. Additionally, shifts in band position and a line broadening are observed after that period (cf. Table I). After a short charging period, two components are again clearly visible in the band profile (trace H). The intensity ratio $I[E_{2g}^{2(i)}]/I[E_{2g}^{2(b)}]$ of the spectra decreases from trace G to trace J. This result is in agreement with the literature and reflects a continuous change of the stage index from 4 to 3 and further towards 2.[10,23] Application of the doublet model to the next spectrum (trace K) shows that the high-wavenumber component (the $E_{2g}^{2(i)}$ mode) of this profile decreases in intensity. It should be mentioned that the signal shown in trace K can also be approximated by using a single Voigt profile centered at 1583 $cm^{-1}$ (cf. Table I). The latter description implies that in this potential region (102–103 mV) the surface consisted of $LiC_{12}$, where only boundary modes should be detectable.[23] The observation that the band profile recorded for the C=O stretching vibration remains unchanged is valid, too, for the subset of spectra shown in traces G to J. However, when the plateau seen at a potential of about 100 mV is reached (cf. Fig. 2A), curve fitting indicates the presence of additional bands in the C=O stretching region. A band detected at about 1850 $cm^{-1}$ rises in intensity with decreasing potential and is strongest for the spectrum recorded at low potential (~5 mV vs. $Li/Li^+$). This band has not yet been described in the literature. A tentative explanation for this band is the formation of complexes between $Li^+$ and EC and/or its decomposition products. As stated above, ethylene evolution is confined to the potential window between about 800 and 300 mV.[16] Thus, the EC decomposition products probably are species originating from oligomerization reactions of EC. Another possible interpretation is associated with the observation of short-range orientation effects in liquid EC,[29] which may be amplified at higher lithium ion concentrations. It has been demonstrated above that the Raman bands of EC change with changing lithium concentration. Finally, we want to point out that this band around 1850 $cm^{-1}$ is observed only in the electrolyte solution very close to the electrode surface.

The formation of $LiC_{12}$ and $LiC_6$ at low potentials results in the disappearance of the band typical for the interior graphene layers. Thus, the spectrum recorded in the low potential range (10–5 mV, trace L) shows no signal in the wavenumber range of the $E_{2g}^{2(b)}$ mode. This phenomenon had already been observed by Inaba et al.[10] and is contrary to the findings of Eklund et al.,[32] who characterized $LiC_6$ and other graphite intercalation compounds (GICs) of various staging indices with Raman spectroscopy. Eklund et al. observed that the Raman band of $LiC_6$ is close in position to the $E_{2g}^{2(b)}$ mode of pristine graphite. To explain this discrepancy, it has been proposed that $LiC_6$, because of its high electrical conductivity, has a very small penetration depth for the excitation laser beam; hence the detection of this band becomes virtually impossible.[10,12] Moreover, Inaba et al.[10] reported a broad band around 1500 $cm^{-1}$. According to the NLLSQ analysis performed on our data, a broad band at 1536 $cm^{-1}$ is found that might be assigned to a lithium-intercalated compound. For GICs of the heavy alkali metals, which have a different stoichiometry (instead of the $MC_6$ compound, $MC_8$ are formed for M = K, Rb, Cs), a broad band is recorded at around 1450–1500 $cm^{-1}$.[23] The experimental results obtained so far suggest the presence of a lithium surface GIC within the penetration depth of the laser that possibly differs in stoichiometry from $LiC_6$.

The Raman spectra recorded during the first discharge half cycle are given in Fig. 7. In reverse order, the same

changes in the Raman spectra are seen as already reported for the first charging half-cycle. Upon discharge, the linewidth of the band at 1536 $cm^{-1}$ gradually decreases (traces A–C), according to results obtained by NLLSQ analysis of the data shown in Fig. 7. These results are compiled in Table II. At potentials >140 mV, a broad profile is observed that is composed of three bands. This profile is observed throughout the potential window from 140 to 240 mV (traces D and E). The broad profile changes in shape and is then composed of two well-resolved lines at potentials >180 mV. Traces F, G, and H in Fig. 7 show these spectra. The intensity ratio $I[E_{2g}{}^{2(i)}]/I[E_{2g}{}^{2(b)}]$ increases in this subset (cf. Table II), as required by the model proposed in Ref. 23. Interestingly, while the linewidth of the $E_{2g}{}^{2(i)}$ mode increases, the linewidth of the $E_{2g}{}^{2(b)}$ mode becomes smaller. This pattern reflects the changes in stacking sequence of the graphene sheets associated with the lithium de-intercalation processes.

The intensity of the band at about 1850 $cm^{-1}$ decreases with increasing potential, its position shifts to higher wavenumber (cf. Table II), and its linewidth decreases. The single line attributed to graphite with low lithium content (dilute stage 1 GIC) is first observed at a potential of 257 mV. In this spectrum (Fig. 7, trace I), and in all spectra recorded at more positive potentials (traces I–K), the band at ~1850 $cm^{-1}$ is no longer visible. This observation suggests that this feature can be assigned to a complex of lithium ions with EC and/or its decomposition products. Upon lithium intercalation, the band at about 1850 $cm^{-1}$ is first observed at a potential of about 100 mV. At this potential, the formation of $LiC_{12}$ is complete, and the formation of $LiC_6$ begins. The concentration of lithium ions in the vicinity of the electrode shows a maximum during this stage, and it will stay at a high level during the de-intercalation process, as long as GIC phases with high lithium content prevail. At potentials positive to ~250 mV, the lithium ion supply from the bulk of the electrode drops off. Finally the electrode surface becomes depleted of lithium ions. According to this model, the formation of the complex between lithium ions and EC is confined to a potential window where large amounts of lithium ions are transported across the interface. It is suggested that the signal at about 1850 $cm^{-1}$ may therefore be used as a marker band for the amount of lithium ions present in the surface region of the electrode.

**Raman Mapping Experiments Performed under *in Situ* Conditions.** *In situ* Raman mapping experiments were performed on the graphite composite electrode. In one type of experiment, the cell was cycled galvanostatically. Other experiments were performed potentiostatically. The results are compared with measurements performed at neat SFG 44 graphite and at as-prepared electrodes (cf. Fig. 4). Before we discuss the results in detail, some remarks about the way data will be represented seem appropriate. A measurement time of 4 min per point had to be used in the acquisition of the data. This condition placed a limitation on the number of points that could be sampled during one mapping experiment, because our experimental setup maintains a stable focus for a period of no more than about 2–3 h. For longer periods, focusing deteriorates because of mechanical vibrations. Currently, this consideration implies that the number of points in one Raman map is limited to about 30–45 points.

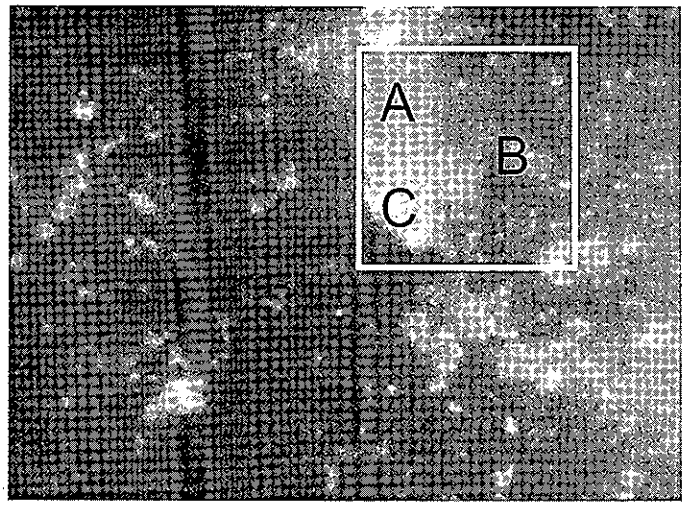


FIG. 8. Video micrograph of the region on the electrode surface used in the potentiostatic mapping experiment. The white bordered square represents an area of 50 μm × 50 μm. The positions of the points where the spectra shown in Figs. 9a and 9b were recorded are indicated by letters.

The results of Raman mapping studies are commonly presented in the form of contour diagrams or a gray scale or color map, where an intensity ratio of two specific bands is plotted to convey the information drawn from the experiment. We decided to illustrate the results using a gray scale map without any interpolation between the points. As mentioned before, the Raman signals are superimposed on a strong background. A background correction has been attempted by using the routines implemented in the software package provided by the manufacturer of the Raman microscope. A polynomial of fourth order was used. Subtraction of the background improved the representation of the data, but inconsistencies arose in the calculation of intensity ratios. Therefore, we decided not to use background-corrected data for the generation of contour maps and used the raw data instead. Just a few spectra will be displayed as examples from the use of background-corrected and normalized data (Figs. 9, 12, and 15).

**Potentiostatic Experiment.** The potentiostatic mapping experiment was performed during the second charging half-cycle at four different electrode potentials. Once the potential had been adjusted to the chosen values, the cell was allowed to equilibrate until the current was lower than 0.1 μA. Raman maps were sampled from the region that is shown in a video micrograph in Fig. 8. The three letters placed into the white frame (dimension 50 μm × 50 μm) represent the location of single-point spectra used to illustrate our results. The spectra taken from the points mentioned were analyzed by using curve fitting; the corresponding results are included in Table III. Since the differences in band position and shape are rather small for the data recorded at 1500 and 800 mV, and therefore of no great interest, only the spectra recorded at potentials of 440 and 200 mV are shown in Figs. 9a and 9b, respectively. The data recorded at 1500, 800, and 440 mV imply a rather homogeneous electrode surface; only the mapping experiment performed at 200 mV revealed dif-

**TABLE III. Band positions and linewidths in spectra recorded for potentiostatic Raman mapping at points indicated (cf Fig. 8). Spectra recorded at 440 and 200 mV are shown in Figs. 9a and 9b. Only results for the bands assigned to graphite and lithium-intercalated graphite are included. The intensity ratio is defined as $I(E_{2g}^{2(i)})/I(E_{2g}^{2(b)})$.**

| Spectrum | Bands assigned to graphite and $Li_xC_y$ | | | Intensity ratio |
|---|---|---|---|---|
| | $E_{2g}^{2(i)}$ | $E_{2g}^{2(b)}$ | $E_{2g}^{2}$ | |
| 1500 mV | | | | |
| A | | | 1580 [21.5] | |
| B | | | 1580 [21.0] | |
| C | | | 1581 [19.2] | |
| 800 mV | | | | |
| A | | | 1580 [22.6] | |
| B | | | 1580 [19.7] | |
| C | | | 1580 [22.0] | |
| 440 mV | | | | |
| A | | | 1584 [16.4] | |
| B | | | 1585 [18.0] | |
| C | | | 1585 [15.8] | |
| 200 mV | | | | |
| A | 1576 [15.1] | 1600 [25.2] | | 14.5:30.7 |
| B | 1579 [26.0] | 1600 [35.2] | | 14.8:21.9 |
| C | 1580 [14.2] | 1585 [50.1] | | 15.5:20.3 |

ferences between band shapes recorded at locations A, B, and C. In the region between 1560 and 1610 $cm^{-1}$, two well-resolved lines appear in trace A of Fig. 9b, a broad signal is observed for trace B, and trace C apparently shows only one band with a shoulder at higher wavenumber. The NLLSQ analysis of these spectra showed that two bands should be employed in describing each profile. According to the data compiled in Table III, traces A and B are spectra of GIC species. From the observation that the intensity ratio $I[E_{2g}^{2(i)}]/I[E_{2g}^{2(b)}]$ is smaller at point A than at point B, we deduce that the extent of lithium intercalation differs between these points. The progress of lithium intercalation at point A is greater that at point B. For trace C in Fig. 9b, the band positions were 1580 and 1585 $cm^{-1}$. These values are typical for pristine graphite or the dilute stage I GIC found at higher potentials. Thus, we wonder when examining the spectrum recorded at point C why a point that showed a normal behavior at 440 mV (band position 1585 $cm^{-1}$, dilute stage I GIC) shows signs of lithium de-intercalation at 200 mV. Nevertheless, it is safe to conclude from the results presented that lithium intercalation does not proceed homogeneously over the electrode surface. It is known that lithium intercalates faster into HOPG single crystals oriented with the edge planes towards the electrolyte [10] Through the basal plane, intercalation can occur only at defect sites.[33] In electrodes with

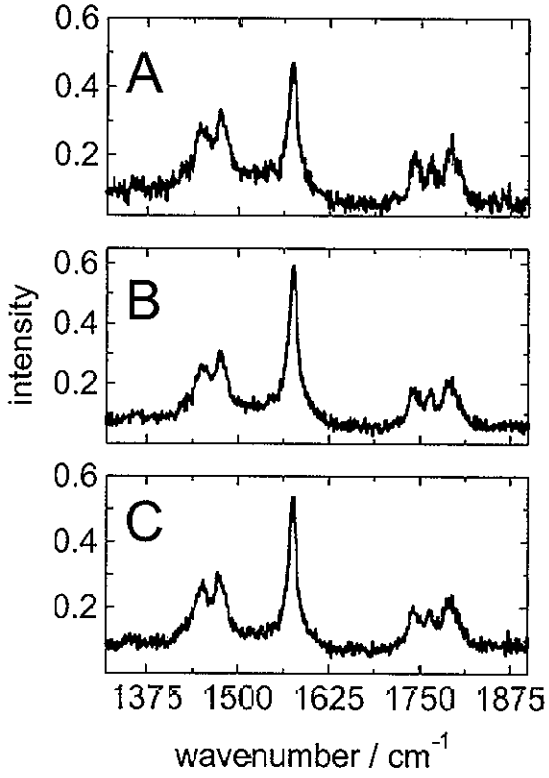


FIG. 9a. Raman spectra recorded in the second cycle at a potential of 440 mV vs. $Li/Li^+$ during charging at the points indicated on the micrograph (Fig. 8).

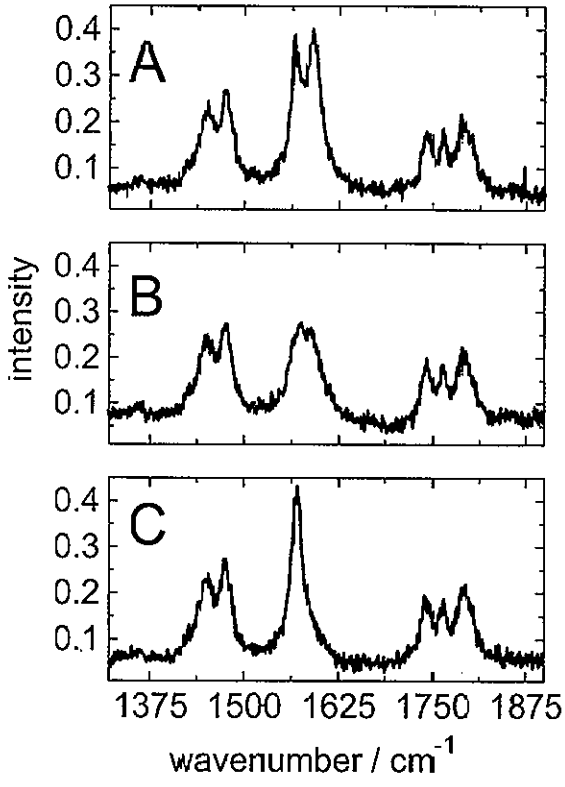


FIG. 9b. Raman spectra recorded in the second cycle at a potential of 200 mV vs. $Li/Li^+$ during charging at the points indicated on the micrograph (Fig. 8).

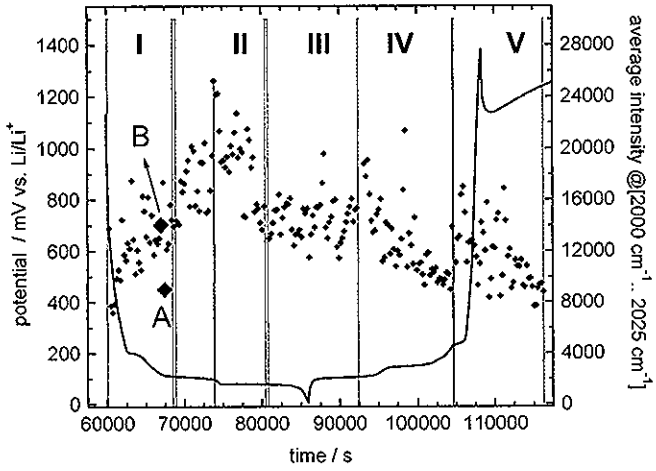


FIG. 10. Charge/discharge curve (solid line, left-hand ordinate) and intensities of the non-Raman background (diamonds, right-hand ordinate) recorded during the second cycle under galvanostatic conditions at 10 μA (~100 μA/mg graphite). Background data shown were derived from raw data. The Roman numbers indicate the windows within which Raman mapping experiments were performed. The letters at the larger-sized diamonds correspond to the points at which the spectra displayed in Fig. 12 were recorded. The current was switched off after charging to 1400 mV.

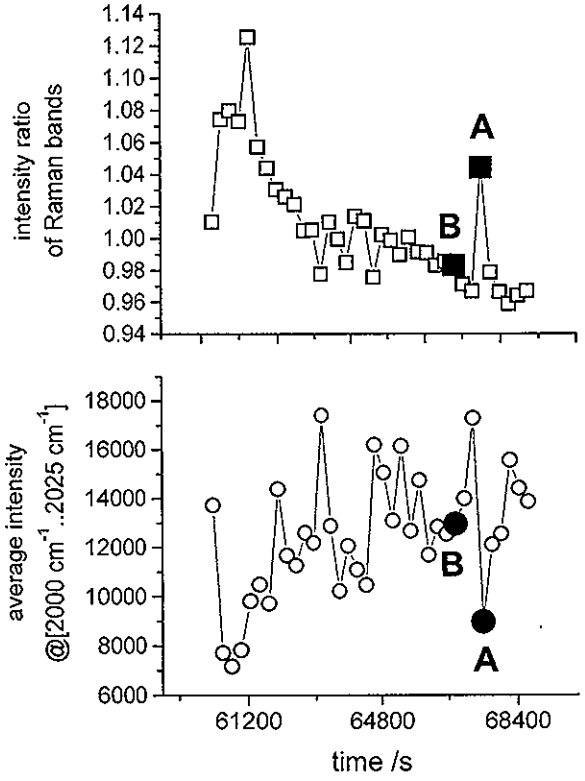


FIG. 11. Non-Raman background intensities (circles) and intensity ratios (squares) against time obtained within potential window I of the galvanostatic curve displayed in Fig. 10. Intensity ratios are calculated by dividing intensity in the bandpass 1570 to 1590 $cm^{-1}$ by the intensity in the bandpass 1650 to 1675 $cm^{-1}$. The letters at the drawn-out symbols mark the data points discussed in the text and correspond to spectra shown in Fig. 12.

a polycrystalline synthetic graphite such as SFG 44, both basal and edge planes will be exposed towards the electrolyte, leading to different lithium intercalation rates at different sites. These kinetic effects may be observed only at potentials where large amounts of lithium are incorporated by the host material. As long as the amount of lithium intercalated is small, as in the formation of the dilute stage I GIC phase, no observable differences exist.

**Galvanostatic Experiments.** Galvanostatic Raman mapping experiments were conducted during the second and third charging/discharging cycle. In the second cycle, a current of 10 μA was used, whereas during the third cycle, the cell was cycled with a current of 40 μA, in order to see whether the occurrence of the band around 1850 $cm^{-1}$ depends on the current density. The galvanostatic mapping experiment has the advantage that, for each point sampled, a fresh surface element is irradiated with the laser beam.

The galvanostatic curve measured during the second cycle is displayed in Fig. 10 (left-hand ordinate). Five Raman maps were collected during this cycle. The potential window of each Raman map can be read from the trace of Fig. 10, by referring to the different sections identified by Roman numbers. The background intensity recorded during the experiment (right-hand ordinate) is shown by diamond symbols, each representing one spectrum. Background intensity is defined as the average intensity in the interval between 2000 and 2025 $cm^{-1}$, where no Raman bands are observed. We recall that the background intensity can be attributed to the PVDF binder and the $LiClO_4$ salt, as shown in Figs. 4 and 5. It emerges from Fig. 10 that the background level increases with the onset of the charging process. A maximum is reached in the potential window corresponding to the transition from $LiC_{12}$ to $LiC_6$. After that, the background slowly decreases. Since no Raman bands of PVDF have been detected in the composite graphite electrode (cf. Fig. 4, spectrum C), we conclude that PVDF is distributed rather homogeneously in the electrode material and the background contribution of PVDF is constant. We therefore attribute the change in background level to changes in lithium salt concentration in the solution very close to the electrode. Support for this conclusion comes from the observation that the background recorded in the bulk electrolyte is constant during the entire charging/discharging process.

The results of the mapping experiment performed in potential window I are shown in Fig. 11. The upper graph contains the sequence of intensity ratios, and the lower figure is constructed from the corresponding background level values defined above (cf. Fig. 10). Intensity ratios were calculated by using the average intensity in the wavenumber interval from 1570 to 1590 $cm^{-1}$, divided by the average intensity recorded in the bandpass from 1650 to 1675 $cm^{-1}$. Comparing corresponding points in the two graphs, we observe a correlation between the two descriptors used. Within the time window shown, the background level increased by a factor of about 2, whereas the intensity ratio decreased by about 10%. With few exceptions, a high intensity ratio is found when the background level is low. Especially noteworthy are the drawn-out data points in the lower right corner, marked with A and B, respectively. Point A represents the 31st spectrum recorded within potential window I, and is shown in Fig. 12, trace A. The Raman spectrum of point B (cf. Fig. 12, trace B) was recorded 12 min earlier, and contains features typical for the intercalation stage reached at this

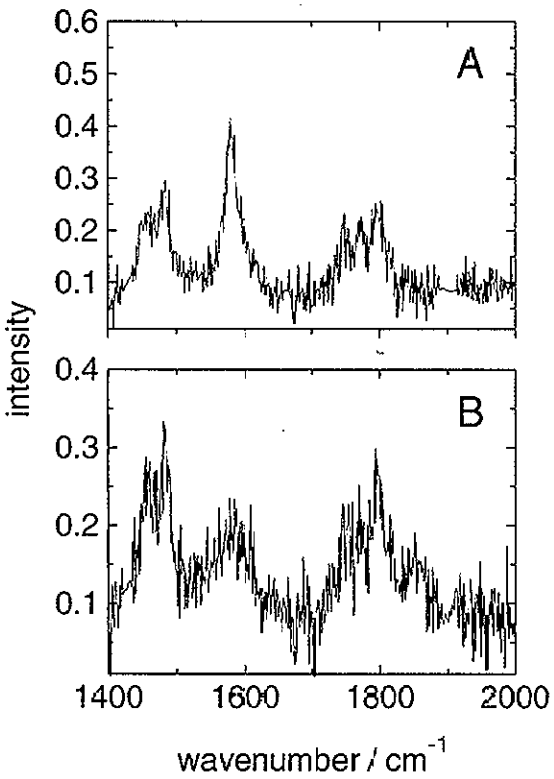


FIG. 12. Raman spectra recorded at the drawn-out points shown in Fig. 11. Spectrum **A** is contrasted with spectrum **B**, which was recorded prior to trace **A** at a slightly higher potential. Both spectra are recorded at potentials of about 100 mV, but the surface point corresponding to the spectrum shown in trace **A** lags behind in the lithium intercalation process.

potential range. Both spectra are recorded in a potential range where spectra of stage 3 or stage 2 should be observed, but from the features in Fig. 12, trace A, only weakly intercalated graphite can be inferred. An intensity ratio that is typical for this phase is observed, together with a distinctly lower background. We suggest as an explanation that, in the absence of a sufficient lithium ion concentration, intercalation takes place at a lower rate. Thus, the point in the lower left corner corresponds to a "blind spot" of the electrode surface, which was detected in the galvanostatic Raman mapping experiment.

The galvanostatic curve recorded in the third cell cycle is shown in Fig. 13. We recall that in this experiment a high current of 40 μA was used. The plateaus corresponding to the different GIC stages are therefore less well resolved, especially in the discharge half-cycle. The background levels calculated in the same way as above are shown as well. There is a striking similarity between the curves recorded during the second and the third cycle. The maximum value of the background is obtained in the same potential window as before. This observation supports the interpretation that has been given above, relating the background level to the lithium ion concentration very close to the surface.

The lower resolution in the galvanostatic curve is mirrored in the Raman spectra recorded during this run, which show no well-resolved features in the potential window corresponding to the transition from stage 4 to stage 2 upon charging. A map of intensity ratios defined as above and obtained during the third cycle is shown in

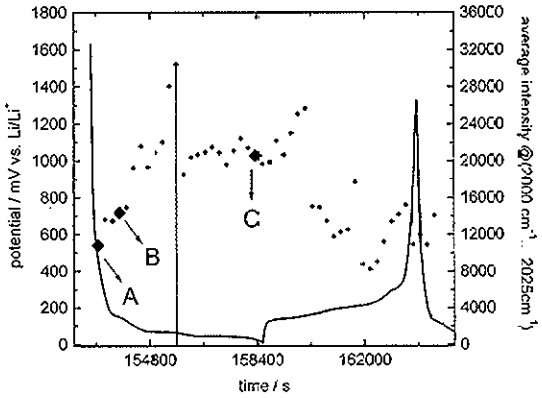


FIG. 13. Galvanostatic curve (solid line, left-hand ordinate) and intensities of the non-Raman background (diamonds, right-hand ordinate) recorded during the third cycle under galvanostatic conditions at 40 μA (~400 μA/mg graphite). Background data shown were derived from raw data. The letters at the larger-sized diamonds correspond to the points at which example spectra were taken (cf. Fig. 15).

Fig. 14. The intensity ratio decreases upon lithium intercalation and increases upon lithium de-intercalation. A complete cycle can thus be described graphically. A few spectra have been selected as examples to illustrate this map. Figure 15, trace A, shows the Raman spectrum recorded at the very start of the experiment. Trace B displays the spectrum recorded at the first distinct plateau below 200 mV. It should be recalled that with a current of 10 μA current in the first cycle, well-resolved spectra were recorded (cf. Fig. 6, traces F, H, and J). Finally, trace C shows the spectrum recorded at the lowest potential. Again, a broad band around 1540 cm$^{-1}$ is observed. Also, the feature around 1850 cm$^{-1}$ is observed at low potential, as in the second cycle (cf. Fig. 12, trace B).

## CONCLUSION

Successful operation of the Raman spectro-electrochemical *in situ* cell designed in our laboratory has been

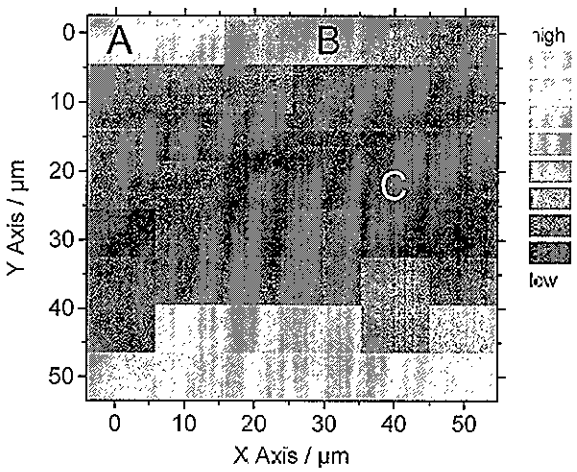


FIG. 14. Raman map obtained from the intensity ratios defined by intensity in the bandpass 1570 to 1590 cm$^{-1}$ over intensity in the bandpass 1650 to 1675 cm$^{-1}$. The letters mark the points for which representative spectra are shown in Fig. 15. A high value of the intensity ratio is typical for the initial and final phase of the charging/discharging cycle, where the $E_{1g}{}^2$ band of carbon is observed.

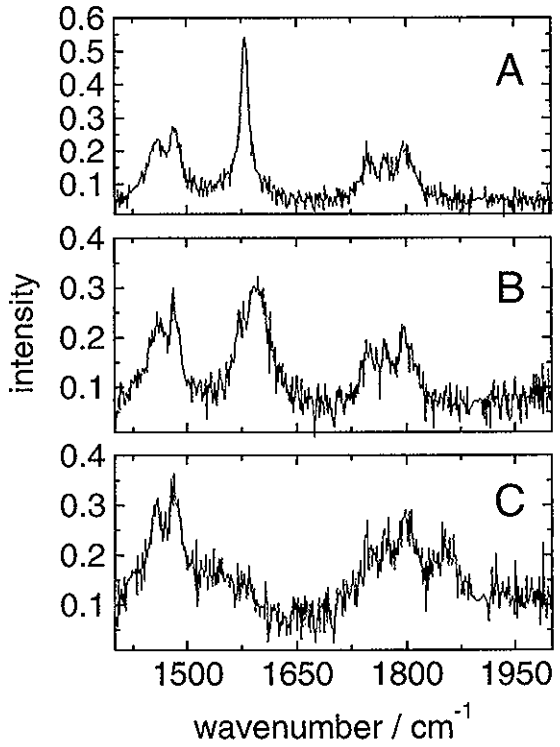


FIG. 15. Selection of Raman spectra recorded during the third cycle at points indicated in Figs. 13 and 14. Spectrum **A** was recorded in the potential window 900–480 mV, whereas spectrum **B** was obtained over the potential range 145–135 mV. Note the feature around 1850 cm$^{-1}$ that is present in trace **C**, recorded at low potential (25 mV).

demonstrated. With our device, the electrode/electrolyte interface can be studied with improved spatial resolution with components used in commercial battery systems. The experiments performed have revealed important changes in the band profile of the C=O stretching region of the electrolyte components in the potential window from about 100 to 5 mV. These changes do occur only in the vicinity of the electrode surface and should therefore be attributed to reversible changes in the structure of the solvent and/or the SEI occurring at high degrees of lithium intercalation; alternatively, the formation of a complex between lithium ions and the EC component of the solvent or its decomposition products might be invoked. We have observed this band during the first, second, and third cycle in our cell. Possibly, this band is useful as a marker band describing the effects of high lithium ion concentration at the electrode surface.

Potentiostatic experiments have been performed in the second cycle. The potentiostatic mapping routine provides a spatially resolved picture of lithium intercalation in a quasi-equilibrium situation. It was found that the intercalation process does not proceed homogeneously over the electrode surface at a potential where larger amounts of lithium ions are transported across the interface. This observation can be related to the structure of the graphite electrode. Both graphite edge planes and basal planes are exposed towards the electrolyte, with edge planes showing faster lithium intercalation rates. It is concluded that differences in lithium intercalations rates are directly related to the differences of spectral features observed. A galvanostatic Raman mapping experiment was performed during the second cycle. A further galvanostatic image was obtained in a third cycle experiment, with a higher charge/discharge rate. The changes in spectral features observed in the C=O region are independent of the current density used. In the galvanostatic experiments, the presence of a "blind spot" has been detected. Within such an area, lithium intercalation is apparently very slow, when compared to neighboring areas. A relation between an intensity ratio determined for the Raman bands of graphite and lithium intercalated graphite, which describes the process of lithium intercalation, and the non-Raman background intensity recorded has been established. With decreasing Raman intensity ratio, the non-Raman background increases. It is thought that the background level yields valuable information about the lithium ion concentration at the electrode/electrolyte interface during the cycle, with higher background level values corresponding to higher lithium ion concentration at the interface.

The measurement time of 4 min per point is rather long and must be reduced significantly by changes in the optical setup before Raman imaging methods can routinely be applied to the generation of Raman maps of reasonable size. But even now, the results obtained in our preliminary Raman mapping experiments are valuable for a characterization of electrodes in lithium-ion cells under operating conditions.

## ACKNOWLEDGMENTS

Thanks are due to Christian Marmy for machining and assembling the parts of the *in situ* cell. Beat Rykart assisted in cell optimization. Werner Scheifele provided technical assistance in the initial phase of the experiments. Financial support from TIMCAL AG, Sins, and the Swiss Federal Office of Energy, Bern, is gratefully acknowledged.

1. J. R. Dahn, A. K. Sleigh, H. Shi, B. M. Way, W. J. Weydanz, J. N. Reimers, Q. Zhong, and U. von Sacken, in *Lithium Batteries: New Materials, Developments and Perspectives*, G. Pistoia, Ed. (Industrial Chemistry Library, Elsevier, Amsterdam, 1994), Vol. 5, Chap. 1.
2. M. Winter, J. O. Besenhard, M. E. Spahr, and P. Novák, Adv. Mater. **10,** 725 (1998).
3. A. Naji, J. Ghanbaja, B. Humbert, P. Willmann, and D. Billaud, J. Power Sources **63,** 33 (1996).
4. K. A. Hirasawa, T. Sato, H. Asahina, S. Yamaguchi, and S. Mori, J. Electrochem. Soc., **144,** L81 (1997).
5. A. C. Chu, J. Y. Josefowicz, and G. C. Farrington, J. Electrochem. Soc. **144,** 4161 (1997).
6. T. Zheng and J. R. Dahn, Synth. Met. **73,** 1, 1995.
7. F. B. Joho, Ph.D. Thesis No. 11745, ETH Zürich (1996).
8. M. D. Levi, E. A. Levi, and D. Aurbach, J. Electroanalytical Chem. **421,** 89 (1997).
9. Y. Matsumura, S. Wang, and J. Mondori, J. Electrochem. Soc. **142,** 2914 (1995).
10. M. Inaba, H. Yoshida, Z. Ogumi, T. Abe, Y. Mizutani, and M. Asano, J. Electrochem. Soc. **142,** 20 (1995).
11. D. E. Irish, Z. Deng, and M. Odziemkowski, J. Power Sources **54,** 28 (1995).
12. W. Huang and R. Frech, J. Electrochem. Soc. **145,** 765 (1998).
13. L. Zhuang, J. Lu, X. Ai, and H. Yang, J. Electroanalytical Chem. **397,** 315 (1995).
14. R. Imhof and P. Novák, J. Electrochem. Soc. **145,** 1081 (1998).
15. R. Imhof and P. Novák, Electrochem. Soc. Proceed. Series PV **97-18,** 313 (1997).
16. J. O. Besenhard and H. P. Fritz, Angew. Chem. Int. Ed. Engl. **95,** 950 (1983).
17. M. D. Levi and D. Aurbach, J. Electroanalytical Chem. **421,** 79 (1997).
18. F. Tuinstra and J. L. Koenig, J. Chem. Phys. **53,** 1126 (1970).
19. R. J. Nemanich and S. A. Solin, Phys. Rev. B **20,** 392 (1979).

20. Y. Wang, D. C. Alsmeyer, and R. L. McCreery, Chem. Mater. **2,** 557 (1990).
21. L. Nikiel and P. W. Jagodzinski, Carbon **31,** 1313 (1993).
22. Y. Kawashima and G. Katagiri, Phys. Rev. B **52,** 10053 (1995).
23. S. Solin, in *Graphite Intercalation Compounds,* Vol. I, H. Zabel and S. Solin, Eds. (Springer Verlag, Berlin, 1990), pp. 178–185.
24. K. Ray III and R. L. McCreery, Anal. Chem. **69,** 4680 (1997).
25. I. Rey, J. C. Lassègues, P. Baudry, and H. Majastre, Electrochim. Acta **43,** 1539 (1998).
26. M. Delhaye, J. Barbillat, J. Aubard, M. Bridoux, and E. Da Silva, in *Raman Microscopy: Developments and Applications,* G. Turell and J. Corset, Eds. (Academic Press, London, 1996), Chap. 3, pp. 66–69.
27. D. I. Ostrovskii, A. M. Yaremko, and I. P. Vorona, J. Raman Spectrosc. **28,** 771 (1997).
28. S. Hyodo and K. Okabayashi, Electrochim. Acta **34,** 1551 (1989).
29. G. Fini, P. Mirone, and B. Fortunato, J. Chem. Soc. Faraday Trans. II **69,** 1243 (1973).
30. Y. T. Lee, J. Raman Spectrosc. **28,** 833 (1997).
31. B. Fortunato, P. Mirone, and G. Fini, Spectrochim. Acta **27A,** 1917 (1971).
32. P. C. Eklund, G. Dresselhaus, M. S. Dresselhaus, and J. E. Fischer, Phys. Rev. B **21,** 4705 (1980).
33. T. D. Tran and K. Kinoshita, J. Electroanal. Chem. **143,** L120 (1996).